

Moisture and the Persistence of Annular Modes

NICHOLAS J. LUTSKO^a AND MOMME C. HELL^a

^a *Scripps Institution of Oceanography, University of California, San Diego, La Jolla, California*

(Manuscript received 26 February 2021, in final form 6 September 2021)

ABSTRACT: Annular modes are the leading mode of variability in extratropical atmospheres, and a key source of predictability at midlatitudes. Previous studies of annular modes have primarily used dry atmospheric models, so that moisture's role in annular mode dynamics is still unclear. In this study, a moist two-layer quasigeostrophic channel model is used to study the effects of moisture on annular mode persistence. Using a channel model allows moisture's direct effects to be studied, rather than changes in persistence due to geometric effects associated with shifts in jet latitude on the sphere. Simulations are performed in which the strength of latent heat release is varied to investigate how annular mode persistence responds as precipitation becomes a leading term in the thermodynamic budget. At short lags (<20 model days, ≈ 4 Earth days), moisture increases annular mode persistence, reflecting weaker eddy activity that is less effective at disrupting zonal-mean wind anomalies. Comparisons to dry simulations with weaker mean flows demonstrate that moisture is particularly effective at damping high-frequency eddies, further enhancing short-lag persistence. At long lags (>20 model days), moisture weakly increases persistence, though it decreases the amplitudes of low-frequency annular mode anomalies. In the most realistic simulation, the greater short-lag persistence increases the e -folding time of the zonal index by 21 model days (≈ 4 Earth days). Moisture also causes a transition to propagating variability, though this does not seem to affect the leading mode's persistence.

KEYWORDS: Annular mode; Atmospheric circulation; Jets

1. Introduction

The annular modes are the leading mode of variability in the extratropical atmosphere of each hemisphere (Thompson and Wallace 2000). They take the form of dipole structures, centered on the time-mean jets and representing north–south fluctuations of the maximum jet speed. With a decorrelation time of 10–30 days, the annular modes are a key source of predictability for midlatitude weather, and their persistence has been linked to the extratropical atmosphere's response to external forcings via the fluctuation–dissipation theorem (FDT) (e.g., Gerber et al. 2008; Ring and Plumb 2008; Lutsko et al. 2015). Qualitatively, a more persistent annular mode may imply a stronger response to external forcing, though applications of the FDT have so far struggled to produce quantitatively accurate estimates of jet responses to forcings (Hassanzadeh and Kuang 2016; Sheshadri and Plumb 2017).

The factors controlling the persistence of annular modes have been extensively studied over the past few decades, with much of this work focusing on the dynamics of a positive eddy feedback which enhances annular mode persistence (e.g., Feldstein and Lee 1998; Robinson 2000; Lorenz and Hartmann 2001; Gerber and Vallis 2007; Simpson et al. 2013; Zurita-Gotor et al. 2014; Zurita-Gotor 2014; Ma et al. 2017; Hassanzadeh and Kuang 2019). These dynamics are complex, involving both barotropic and baroclinic components, and the strength of the feedback is difficult to quantify: Byrne et al. (2016) demonstrated that some of the statistical methods previously used to measure the eddy feedback cannot unambiguously

distinguish between an internal eddy–jet feedback and a low-frequency external forcing.

Robinson (2000) proposed a dynamical framework for understanding the positive eddy feedback which includes both barotropic and baroclinic aspects. Robinson's mechanism begins with anomalous upper-level eddy momentum fluxes inducing a barotropic wind anomaly. Zonal-mean baroclinicity is then generated as friction damps the lower-layer winds, which leads to locally enhanced eddy generation and hence to enhanced eddy momentum convergence, reinforcing the original zonal wind anomaly. Subsequent studies of idealized simulations and observations have investigated the damping of the baroclinic anomaly by the combined effects of downgradient eddy heat fluxes and diabatic heating (Blanco-Fuentes and Zurita-Gotor 2011; Zurita-Gotor et al. 2014; Hassanzadeh and Kuang 2019), and have also emphasized the strong covariance of annular modes and baroclinicity anomalies. However, despite these advances in our understanding of the internal dynamics of annular mode variability, it is still an open question whether baroclinic or barotropic dynamics are the primary driver of the variability—see Jin et al. (2006b,a) and Barnes and Hartmann (2011) for examples of how annular mode dynamics can be understood from purely barotropic points of view.

Interactions with other modes of variability may also affect annular mode persistence. These modes become more prominent when jet variability is dominated by poleward propagating mean-flow anomalies—i.e., by propagating modes (Feldstein and Lee 1998; Sheshadri and Plumb 2017)—rather than by meridional oscillations about the jet axis. Lubis and Hassanzadeh (2021) have recently shown that a cross-EOF feedback between the two leading modes of variability can reduce annular mode persistence in the propagating regime, but while

Corresponding author: Nicholas Lutsko, nlutsko@ucsd.edu

DOI: 10.1175/JAS-D-21-0055.1

© 2021 American Meteorological Society. For information regarding reuse of this content and general copyright information, consult the AMS Copyright Policy (www.ametsoc.org/PUBSReuseLicenses).

Brought to you by NATIONAL TAIWAN UNIV | Unauthenticated | Downloaded 11/15/23 01:44 AM UTC

they proposed a framework for modeling cross-EOF feedbacks, the dynamics of these feedbacks are still unclear.

These insights into annular mode dynamics have come primarily from idealized dry models, including relatively simple two-layer quasigeostrophic (QG) and stirred barotropic models, as well as multilevel primitive equation models. Even observational studies have approached annular mode dynamics from a “dry” perspective (e.g., [Blanco-Fuentes and Zurita-Gotor 2011](#)). So, despite significant progress in understanding the dynamics of annular modes, it is still unclear how moisture affects jet variability [though we note that [Xia and Chang \(2014\)](#) have attempted to mimic moisture’s effects in a dry model].

As a first step toward addressing moisture’s role in annular mode dynamics, the present study investigates the persistence of annular modes in a two-layer QG channel model to which a representation of moist processes is added. Two-layer QG channel models can produce realistic annular mode-like behavior, and the model’s symmetry means that annular mode persistence is not affected by shifts in the mean latitude of the jet: the presence of moisture tends to shift jets poleward ([Frierson et al. 2006](#)), and jets that are further poleward tend to have reduced persistence. [Barnes and Hartmann \(2010\)](#) explained the impact of changes in latitude on persistence by noting that Earth’s sphericity inhibits wave breaking on the poleward flanks of eddy-driven jets, hence the feedback between eddies and the mean-flow weakens as the jet moves poleward. Using a channel model eliminates this “geometric” effect, isolating moisture’s “direct” effects on annular mode persistence.

The moist two-layer QG model used here is similar to the model developed by [Lapeyre and Held \(2004\)](#), who considered a setup with a meridionally uniform mean flow, and several follow-up studies continued the investigation of the dynamics of moist two- and three-layer QG and shallow water models ([Bouchut et al. 2009](#); [Lainé et al. 2011](#); [Lambaerts et al. 2011b,a, 2012](#)). Recently, [Bembenek et al. \(2020\)](#) relaxed the flow in a moist two-layer shallow water model to a Bickley jet, which produces a climate that resembles the observed mid-latitude circulation. Adding moisture in their setup pushes the jet poleward and weakens eddy activity, because precipitation acts as an energy sink, reducing the conversion of zonal-mean available potential energy (APE) into eddy APE, and in turn the conversion of eddy APE into eddy kinetic energy (EKE). Note that warming experiments, with varied SSTs or CO₂ concentrations, represent more general perturbations, with other important effects in addition to changes in moisture (e.g., changes in meridional temperature gradients). Thus the results of warming experiments and dry/moist experiments are not directly comparable.

Here we use a moist two-layer QG model, rather than a moist two-layer shallow water model, to investigate moisture’s impact on jet variability. As in [Lapeyre and Held \(2004\)](#) and [Bembenek et al. \(2020\)](#), we vary the strength of latent heat release, which causes the model to transition from a “weak” moisture to a “strong” moisture regime. The latter is dominated by cyclones and is similar in some respects to the “TC worlds” seen in simulations of rotating radiative–convective

equilibrium (e.g., [Held and Zhao 2008](#); [Zhou et al. 2017](#)). Pushing the model into the strong moisture regime allows us to explore annular mode behavior when precipitation is a leading term in the thermodynamic balance.

More details on the moist two-layer QG model are provided in the following section, and the effects of adding moisture on the mean climate and variability of the model are described in [section 3](#). The changes in short-lag and long-lag persistence are discussed in more detail in [section 4](#), and [section 5](#) compares the moist simulations to dry simulations with weaker mean flows. [Section 6](#) investigates the transition to propagating variability which is seen as the strength of latent heating is increased, before we end with conclusions in [section 7](#).

2. Model formulation

a. Dry model

The “dry” two-layer QG model consists of two constant density layers on a β plane in which the meridional temperature gradient (i.e., the slope of the interface) is relaxed toward an equilibrium profile. The layers have equal depths and bottom friction is present in the lower layer. The nondimensional equations¹ are

$$\begin{aligned} \frac{\partial q_k}{\partial t} + J(\psi_k, q_k) = & -\frac{1}{\tau_d}(-1)^k(\psi_1 - \psi_2 - \psi_R) \\ & -\frac{1}{\tau_f}\delta_{k2}\nabla^2\psi_k - \nu\nabla^4q_k, \end{aligned} \quad (1)$$

where $q_k = \nabla^2\psi_k + (-1)^k(\psi_1 - \psi_2) + \beta y$ is the potential vorticity (PV) in the upper ($k = 1$) and lower ($k = 2$) layers, the ψ_k variables are the streamfunctions, τ_d is a Newtonian relaxation time scale, τ_f is a Rayleigh friction time scale acting only in the lower layer, and ν is a hyperdiffusion coefficient.

The model domain is a zonally periodic channel, with a baroclinic zone in the center of the domain created by relaxing the model’s temperature gradient $[(\partial/\partial y)(\psi_1 - \psi_2)]$ to an equilibrium profile ψ_R consisting of a hyperbolic secant centered at $y = 0$:

$$-\frac{\partial\psi_R}{\partial y} = A \operatorname{sech}^2(y/\sigma), \quad (2)$$

where A is set to 1 in most experiments (though see [section 5](#)) and σ controls the width of the jet.

The maximum strength of the vertical shear of the zonal wind in radiative equilibrium is used as the velocity scale (U) in nondimensionalizing these equations, while the length scale (λ) is the deformation radius. The model’s time scale is then λ/U , which we refer to as a model day, although it is only equal to roughly 1/5 of an Earth day for plausible choices of L and U .

The control parameter settings are similar to [Lutsko et al. \(2015\)](#): $\beta = 0.2$, $\sigma = 3.5$, $\tau_f = 15$, $\tau_d = 100$, and $\nu = 10^{-6}$.

¹ There is no unambiguously optimal choice of parameters for the model that provides the best comparison with observations, so all results are reported nondimensionally.

The code is spectral in both x and y , and sponges prevent eddies from growing on the boundaries. All simulations are conducted in a domain with zonal length $L_x = 46$ and meridional width $L_y = 96$, with 128 wavenumbers retained in both dimensions.

b. Adding moisture

Moisture is added as an active tracer in the lower layer, similar to [Lapeyre and Held \(2004\)](#), though with some differences, as we relax the interface slope to an equilibrium profile rather than prescribing a uniform background wind. The moisture variable m represents a mixing ratio that has been nondimensionalized using the scale $m_0 U / (f_0 \lambda)$, where m_0 is a reference lower-tropospheric mixing ratio, which we set to 10 g kg^{-1} . The equation for m is

$$\frac{\partial m}{\partial t} + J(\psi_2, m) = E - P - \nabla \cdot \mathbf{u}_2, \quad (3)$$

where E is surface evaporation and P is precipitation. The last term on the right-hand side is a linearization of the *ageostrophic* advection in the lower layer, which is required for consistency with the QG framework.

To calculate P and E , a saturation moisture concentration m_s is defined as

$$m_s = C(\psi_1 - \psi_2), \quad (4)$$

where C is a constant. Equation (4) can be thought of as a linearization of the Clausius–Clapeyron relation, where C is related to the coefficient relating temperature and saturation vapor pressure. Precipitation instantaneously resets m to m_s wherever $m > m_s$:

$$P = \begin{cases} (m - m_s)/\tau_p & \text{if } m > m_s, \\ 0 & \text{if } m \leq m_s, \end{cases} \quad (5)$$

with τ_p set to 1. Evaporation is calculated using a “bulk formula” wherever the moisture is subsaturated:

$$E = \begin{cases} \hat{E} |\mathbf{u}| (m_s - m) & \text{if } m < m_s, \\ 0 & \text{if } m \geq m_s, \end{cases} \quad (6)$$

with \hat{E} a constant of proportionality.

Finally, in the presence of moisture the “dry” PV equations are modified to

$$\begin{aligned} \frac{\partial q_k}{\partial t} + J(\psi_k, q_k) &= -\frac{1}{\tau_d} (-1)^k (\psi_1 - \psi_2 - \psi_R) - \frac{1}{\tau_f} \delta_{k2} \nabla^2 \psi_k \\ &\quad - \nu \nabla^4 q_k + (-1)^k LP, \end{aligned} \quad (7)$$

where L controls the strength of latent heating. Hence precipitation effectively moves mass from the upper layer to the lower layer.

The moisture variable adds four free parameters: C , L , τ_p , and \hat{E} . [Lapeyre and Held \(2004\)](#) estimated realistic values for C and L of 2 and 0.2, respectively, and, as stated above, τ_p is set equal to 1. We set $\hat{E} = 0.1$, which is equivalent to a bulk transfer coefficient of $\approx 10^{-7} \text{ m}^{-1}$ —comparable to the value in [Bembenek et al. \(2020\)](#).

TABLE 1. List of experiments and e -folding times for the leading mode of variability.

Expt	e -folding time (model days)
$L = 0.0, A = 1$	39
$L = 0.1, A = 1$	50
$L = 0.2, A = 1$	56
$L = 0.3, A = 1$	60
$L = 0.4, A = 1$	64
$L = 0.5, A = 1$	67
$L = 0.0, A = 0.9$	43
$L = 0.0, A = 0.8$	45

With the estimated value for the latent heating coefficient in mind, we have varied L from 0 to 0.5 in increments of 0.1, which takes the model from a dry climate to a climate that approaches the “strong latent heat release” regime (see [Table 1](#)). Testing indicated that larger values of L lead to a climate without a well-defined jet, and even for $L = 0.5$ the poleward flank of the jet is very broad (see [Fig. 1a](#)).

Each experiment was run for 101 000 model days, equivalent to 20 200 Earth days, with data recorded once per model day and the first 1000 days discarded as spinup. To calculate the precipitation and evaporation, the time-stepping procedure has to be modified from the original dry model, and the approach taken here is described in the [appendix](#).

3. Mean state and variability of the moist QG model

a. Mean state

We begin the presentation of our results by briefly describing how the mean state of the model is affected by the presence of moisture. The control “dry” climate has been discussed in other studies (e.g., [Zurita-Gotor et al. 2014](#); [Lutsko et al. 2015](#); [Lutsko et al. 2017](#)), and consists of a strong equivalent barotropic jet, centered in the middle of the domain (black curves in [Figs. 1a,b](#)). There are weaker jets on the shoulders of the main upper-layer jet, centered at $y = \pm 9$, and eddies converge zonal momentum into the jet ([Fig. 1c](#)) and transport heat poleward across the jet in the upper layer ([Fig. 1d](#)).

The changes in the model’s climate as L is varied are generally consistent with [Bembenek et al. \(2020\)](#). The jet progressively shifts poleward, widens, and weakens as L is increased, and this is associated with northward displacement and weakening of the eddy momentum fluxes (EMFs), the eddy heat fluxes (EHFs), and the EKE ([Figs. 1c–e](#), see also [Fig. 2](#)). [Bembenek et al. \(2020\)](#) did not observe such a clear weakening of the jet, though they did find reductions in the EMFs, and they did not show the zonal-mean winds for strong moisture cases. Nevertheless, it is possible that jets in shallow water models are less prone to decelerating in the presence of moisture. As mentioned in the introduction, studies with idealized general circulation models have also shown poleward jet shifts in the presence of moisture ([Frierson et al. 2006](#)).

Precipitation peaks on the poleward flank of the jet ([Fig. 1f](#)), and forms as air is advected poleward and its relative humidity increases, similar to warm conveyor belts, which produce precipitation on the

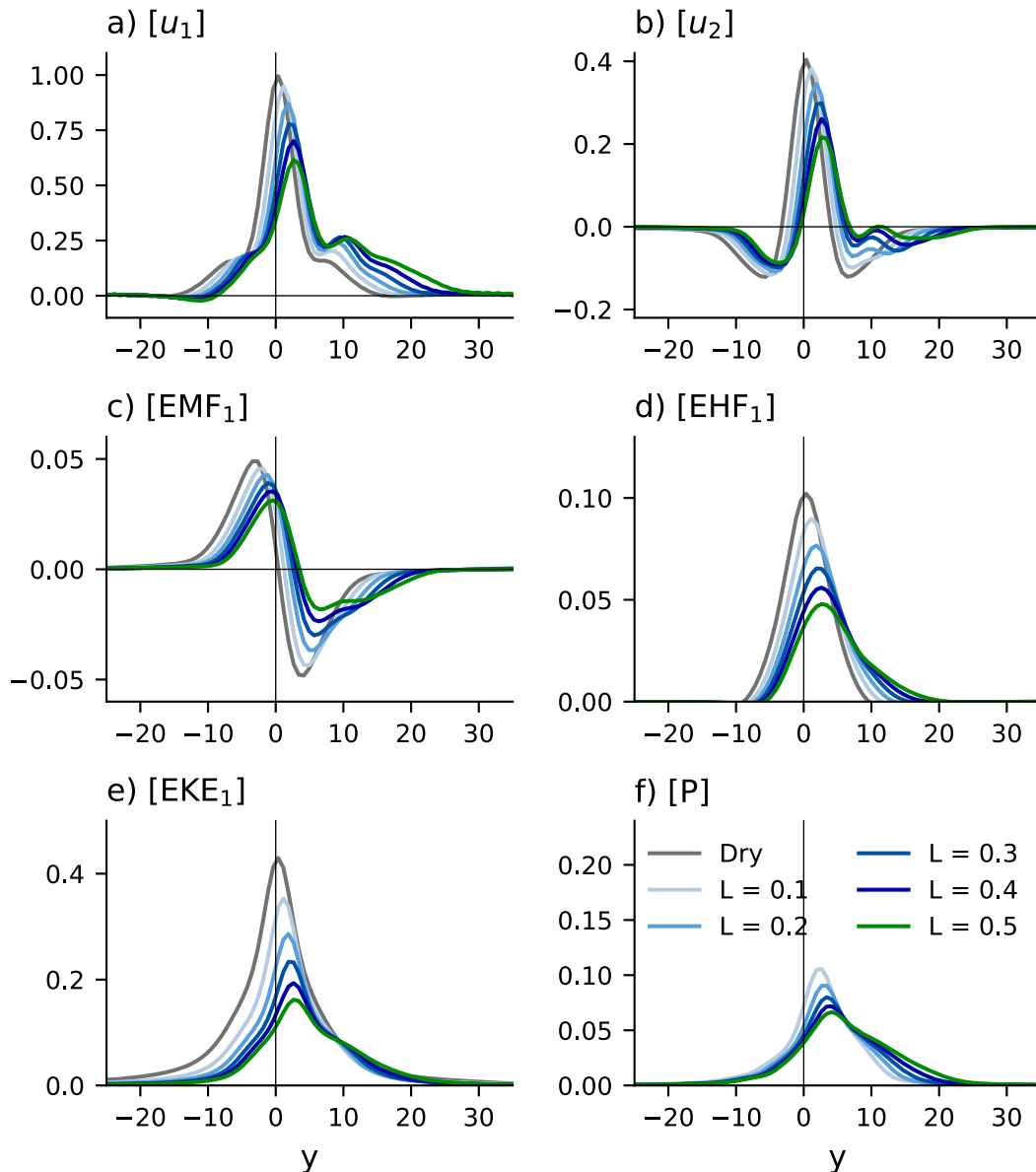


FIG. 1. Dry and moist climatologies for the zonal-mean zonal wind in the (a) upper layer ($[u_1]$) and (b) lower layer ($[u_2]$), (c) the upper-layer zonal-mean eddy momentum fluxes ($[EMF_1]$), (d) the upper-layer zonal-mean eddy heat fluxes ($[EHF_1]$), (e) the upper-layer zonal-mean eddy kinetic energy ($[EKE_1]$), and (f) the zonal-mean precipitation ($[P]$).

poleward flanks of midlatitude storms (Wernli and Davies 1997; Chang and Song 2006). Since the precipitation is concentrated on the poleward side of the jet, the associated latent heat release in the lower layer weakens the baroclinicity and pushes the baroclinic zone poleward. In turn, the jet also weakens and shifts poleward, though the jet changes are mediated by eddies (e.g., the weaker EMFs). A more in-depth investigation of how jets respond to the presence of moisture is left for future work.

b. Variability

The leading mode of zonal-wind variability in every simulation is a meridional displacement of the jet, representing

annular-mode like variability (Fig. 3a). The modes are centered at the location of maximum jet speed and shift poleward as L is increased, but the shapes of the modes are very similar.² Note that while these leading EOFs resemble the commonly derived dipole structure about the time-varying zonal-mean zonal jet (Hartmann and Lo 1998; Lorenz and Hartmann 2001; Monahan and Fyfe 2006), they have a more complex structure

² Although not shown here, the meridional structure of the lower-layer EOF is also similar, apart from shifting poleward as L is increased.

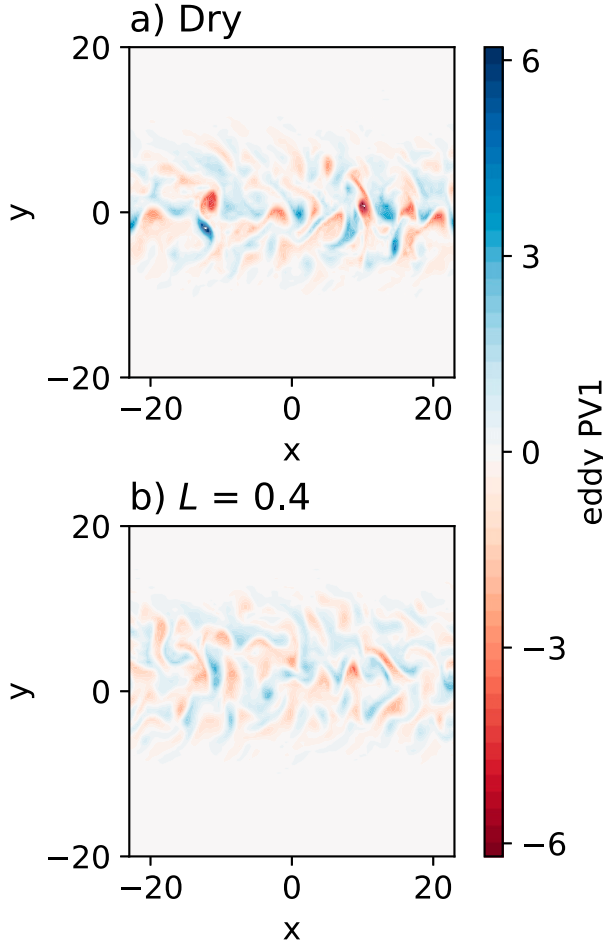


FIG. 2. Snapshots of the upper-layer eddy potential vorticity (a) in the control simulation and (b) in the simulation with $L = 0.4$.

than an isolated dipole (Fig. 3a). This stems from the fact that the jets have more than two local maxima, and hence their shapes differ from a generic Gaussian (Fig. 1a; Monahan and Fyfe 2009).

The persistence of the annular modes increases at all lags as L is increased, with the e -folding time of the zonal index (z_1 , the principal component associated with the leading EOF) increasing from 39 model days for $L = 0$ to 67 model days for $L = 0.5$ (Table 1, Fig. 4a). The probability density function (PDF) of z_1 also contracts as L is increased (Fig. 3d), indicating smaller meridional displacements of the jet, or else that larger displacements are captured by higher EOFs.

To describe this behavior in a different way, we use the zonal index model of Lorenz and Hartmann (2001):

$$\frac{\partial z_1}{\partial t} \approx \mu - \frac{z_1}{\tau_z}, \quad (8)$$

where μ is the forcing by the vertically integrated EMFs and τ_z is the time scale of the effective barotropic friction ($\approx 2.7\tau_f$ for the control simulation, see discussion in section 4b). Lorenz and Hartmann (2001) showed that the spectrum of μ displays enhanced power at low frequencies, which can be modeled as a linear

feedback: $\mu = \gamma z_1 + \hat{\mu}$, where $\hat{\mu}$ is the part of the eddy forcing independent of z_1 and γ is a feedback coefficient. Substituting into Eq. (8), the persistence of z_1 decays at long lags as a red-noise process, with a reduced damping scale $\alpha = \gamma - 1/\tau_z$.³

The key features of the Lorenz and Hartmann model can be seen in the autocorrelation of z_1 in the dry simulation ($C_{z_1 z_1}$, dark gray curve in Fig. 4a). Initially, the autocorrelation drops off rapidly due to the noisy forcing ($\hat{\mu}$), but then the persistence of z_1 is enhanced at lags of $\sim \pm 15$ model days by the positive feedback. These regimes can be identified more clearly by examining the decay rate $d\log(C_{z_1 z_1})/d\tau$, which in the absence of an eddy feedback would be equal to $1/\tau_z$ at long lags [see Eq. (6) of Zurita-Gotor et al. 2014]. Figure 4c shows that $C_{z_1 z_1}$ decays more slowly at short lags as L is increased, but is very similar in all of the simulations between lags of 25–60 days. Beyond 60 days the decay rates are noisy.

These results suggest that the short-lag persistence is enhanced as L is increased, but that the long-lag persistence is roughly constant. It is still an open question how best to quantify the eddy feedback (Byrne et al. 2016; Ma et al. 2017), and we have used both the Lorenz and Hartmann (2001) method and the Simpson et al. (2013) method to estimate γ . The former measures γ as the value which minimizes the lagged correlation between z_1 and μ for moderate and large lags [see Lorenz and Hartmann (2001) for more details], while the latter estimates γ using lag regressions as $\gamma = \text{regr}(\mu, z_1)/\text{regr}(z_1, z_1)$, where $\text{regr}(\mu, z_1) = \sum_l \mu(t+l) \times z_1(t)$ and l is a given lag. In this model, where there is no variability external to the jet, neither method is subject to the misinterpretations identified by Byrne et al. (2016).

In both methods, the choice of lag is crucial, as it must be long enough that the influence of the random eddy forcing is roughly zero [$\text{regr}(\hat{\mu}, z_1) \approx 0$ for large-enough l], but also short enough that sampling errors are small. In their analysis of reanalysis data and of an idealized primitive equation model, Simpson et al. (2013) used lags of 8–20 Earth days to estimate the eddy feedback, while Lorenz and Hartmann (2001) used a lag of 7 Earth days. Based on the $d\log(C_{z_1 z_1})/d\tau$ curves in Fig. 4c, we have estimated γ using both techniques for lags of 30–60 model days, then averaged over the results. Both methods give values of $\gamma \approx 0.012$ – 0.018 (Fig. 5), and suggest that the feedback strengthens for larger L , though the changes are nonmonotonic and small relative to the sampling error. Although we are not confident in the statistical robustness of these changes, in section 4b we provide further support for the apparent increase in γ with L .

c. Higher modes of variability

The variance explained by the leading zonal-mean zonal wind EOF decreases from 41% to 27% across the simulations, which is compensated by increases in the variance explained by higher EOFs (Fig. 3c). The spatial structure of the second EOF is similar in the dry and moist simulations, apart from meridional shifts, and represents a pulsing of the maximum jet speed

³ We assume that α is constant, though it is more accurate to think of it as changing with frequency (Zurita-Gotor et al. 2014; Ma et al. 2017).

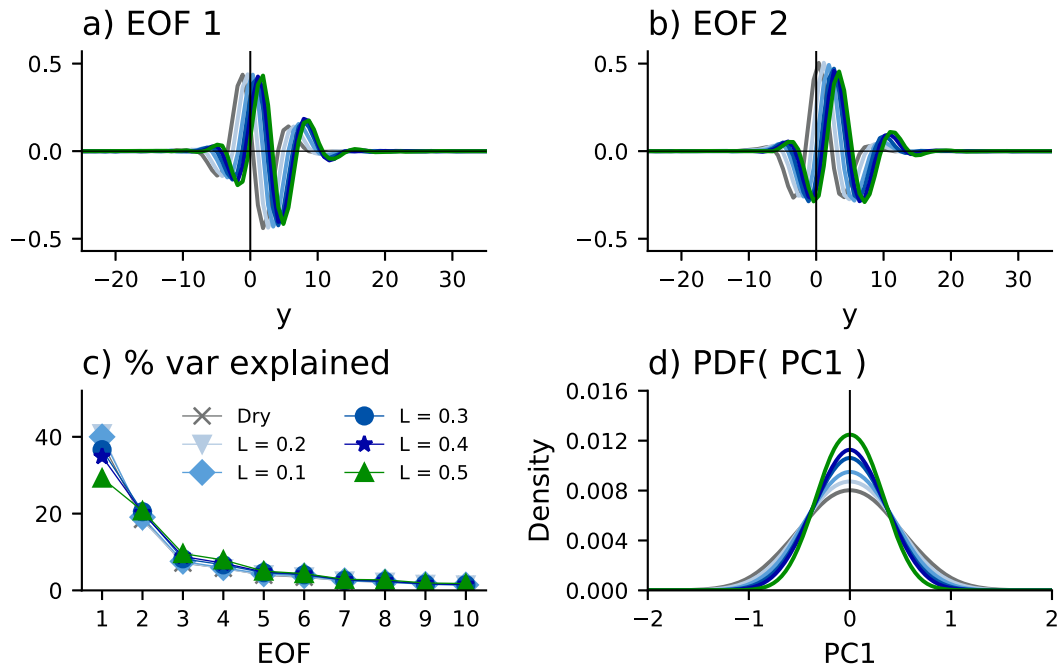


FIG. 3. (a) Leading EOF of the upper-layer zonal-mean zonal winds in the simulations with $L = 0$ to 0.5. (b) EOF 2 of the upper-layer zonal-mean zonal winds in the same simulations. (c) Percentage variance explained by the first 10 EOFs in the simulations with varying L . The first 10 EOFs are well-resolved in every simulation according to the North et al. (1982) criterion. (d) Probability density functions of the zonal index in the same simulations.

(Fig. 3b). As L increases, the second EOF's principal component becomes more persistent (Fig. 4b), and its lag cross correlation with the first principal components also increases (Fig. 4d). The enhanced persistence and lagged cross correlation suggest a transition to a propagating annular mode regime for large L (section 6; Feldstein and Lee 1998; Sheshadri and Plumb 2017). We have not investigated what causes the transition to propagating variability for large L , but note that wider jets with weaker potential vorticity gradients favor propagating modes (Son and Lee 2006; Son et al. 2008; see Fig. 1a).

4. Understanding the changes in persistence

a. Changes in short-lag persistence

To interpret changes in short-lag persistence as L is increased, we use the Wiener-Khinchin theorem, which states that the power spectra of the zonal index z_1 and its forcing μ are equivalent to the Fourier transforms of their autocorrelations. Equation (8) can thus be used to relate the power spectrum of z_1 to the power spectrum of μ :

$$P_z(\omega) = \frac{P_\mu(\omega)}{\tau_z^{-2} + \omega^2}. \quad (9)$$

The power spectra P_μ in the dry and moist simulations are shown in Fig. 6a. All spectra exhibit a peak at high frequencies [10–100 (model day)^{−1}], a minimum near 200–400 (model day)^{−1}, and enhanced power at low frequencies [>400 (model day)^{−1}]. In the dry case, the high-frequency peak has a much larger amplitude than the low-frequency peak and dominates

the short-lag response of z_1 , implying fast decay of the autocorrelation. As L is increased, the power at high frequencies decreases faster than the power at low frequencies, such that for $L = 0.5$ there is relatively more power at low frequencies, implying slower decay of the autocorrelation at short lags. The weaker high-frequency eddy forcing is a result of the weakening of eddy activity as L is increased, which is thus partly responsible for the zonal index becoming more persistent at short lags (though see further discussion in section 5).

The response to increasing L is in contrast to what is seen in simulations with varying friction. Zurita-Gotor (2014) showed that P_μ is roughly constant as τ_f is varied, so that changes in persistence are solely determined by changes in friction. To confirm that the changes in short-lag persistence are not driven by large changes in the effective barotropic friction τ_z , we estimate τ_z in the various simulations by noting that at low frequencies Eq. (9) reduces to

$$P_z(\omega) \approx \tau_z^2 P_\mu(\omega). \quad (10)$$

Thus the ratio of P_z to P_μ at low frequencies is approximately equal to τ_z^2 . Figure 6b shows that in all of the experiments P_z/P_μ asymptotes at low frequencies to a similar value of $\tau_z \approx 2.7\tau_f \approx 40.5$ model days, confirming that changes in the effective friction are small across the experiments, and that the increases in short-lag persistence reflect weakening of the eddy momentum forcing.

b. Changes in long-lag persistence

The feedback analysis in section 3b suggests that the low-frequency eddy feedback γ increases with L , but the changes

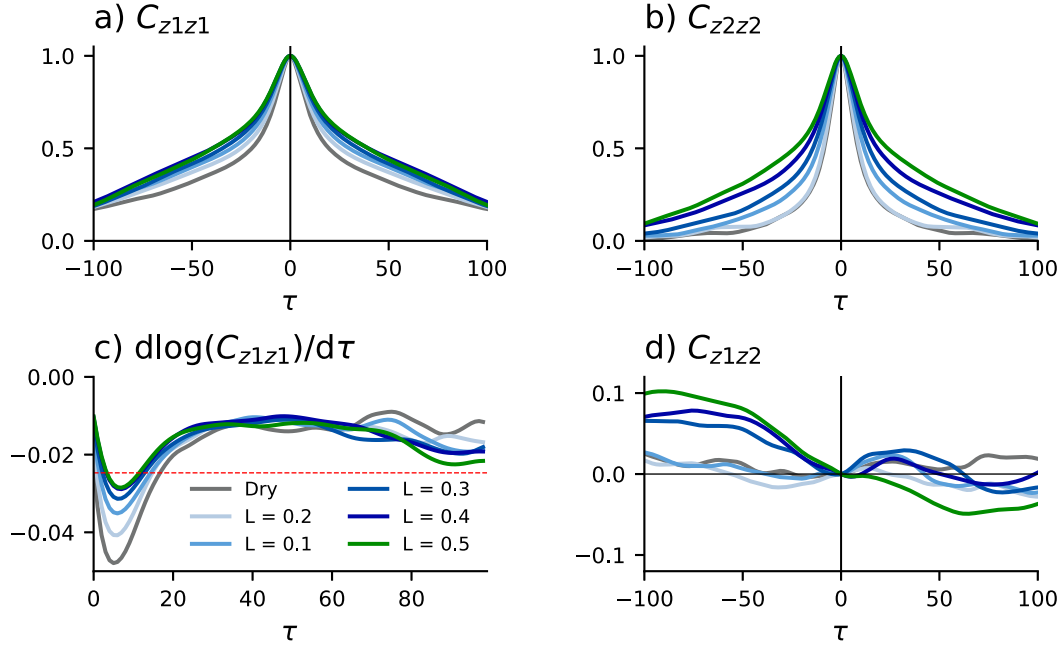


FIG. 4. (a) Autocorrelation of the zonal index (C_{z1z1}) as a function of lag τ in the simulations with $L = 0$ to 0.5. (b) Autocorrelation of the principal component associated with EOF2 (C_{z2z2}) as a function of lag τ in the same simulations. (c) $d\log(C_{z1z1})/d\tau$ in the same simulations. The dashed red line shows the decay rate implied by the frictional time-scale τ_z . (d) Cross correlation of the two leading principal components in the same simulations.

are not statistically robust. Further evidence for increases in γ comes from examining τ_z more closely. From Eq. (8) and the discussion in section 3b, at low frequencies, when the noisy eddy forcing $\hat{\mu} \approx 0$, $\mu \approx z_1/\tau_z \approx \gamma z_1$. Thus the low-frequency eddy feedback scales as $\gamma \sim 1/\tau_z$, and the small increases in γ should correspond to small decreases in τ_z .

Figure 6b suggests that changes in τ_z are small, but the ratio of P_z to P_μ is only approximately equal to τ_z . The effective barotropic friction can be estimated more accurately by taking the ratio of the projection of the barotropic wind onto the leading barotropic wind EOF to the projection of the lower-layer wind onto the leading barotropic wind EOF (Lorenz and Hartmann 2001). Consistent with the slight increase in γ , we find that τ_z decreases from $\sim 2.7\tau_f$ to $\sim 2.6\tau_f$ across the simulations (not shown), suggesting that the variability becomes slightly more barotropic as L is increased, which weakens τ_z and strengthens the eddy feedback slightly. The decreases in τ_z counter the increases in γ , leaving the total damping rate α unchanged.

It is surprising that the changes in γ are small, given the large changes in baroclinicity when moisture is added to the model. The relative insensitivity of γ to moisture indicates that baroclinic dynamics are not the primary driver of changes in low-frequency persistence. To explore this further, in the next section, we examine life cycles of the leading modes of shear and baroclinicity variability to understand how the Robinson feedback mechanism responds as L is increased.

c. Baroclinicity and shear anomaly life cycle analysis

Previous work has used the life cycles of baroclinicity and shear anomalies to investigate the dynamics of the Robinson

feedback mechanism in idealized QG models (Zurita-Gotor et al. 2014) and in reanalysis products (Blanco-Fuentes and Zurita-Gotor 2011). Here we use life cycle analysis to understand how the dynamics underlying the positive eddy feedback γ respond to changes in L .

The leading modes of the vertical wind shear and of the baroclinic variability consist of meridional shifts of the maximum wind shear and of the baroclinicity, respectively. An equation for the zonal-mean vertical wind shear $[u_1] - [u_2]$ can be constructed as in Zurita-Gotor et al. (2014):⁴

$$\frac{\partial s}{\partial t} \approx F(u'v') + F(\text{MMC}_U) + \frac{s}{\tau_f}, \quad (11)$$

where $s = \int ([u_1] - [u_2]) \cdot \mathbf{v}_s dy$, $F(u'v') = -\int \partial[u'_1 v'_1 - u'_2 v'_2]/\partial y \cdot \mathbf{v}_s dy$ is the eddy momentum forcing and $F(\text{MMC}_U) = \int [v_a] \cdot \mathbf{v}_s dy$ is the forcing by the mean meridional circulation (MMC), with v_a the ageostrophic meridional velocity in the upper layer, and the vector \mathbf{v}_s is the leading EOF of the vertical wind shear. Square brackets denote zonal means, and F denotes forcing functions. Note that no new terms are added to Eq. (11) in the presence of moisture.

An equation for the baroclinicity shift can be similarly obtained by projecting the y -differentiated thermodynamic equation onto the leading baroclinicity EOF, which gives (Thompson and Barnes 2014; Zurita-Gotor et al. 2014)

⁴ Hyperdiffusion is ignored in this approximate expression.

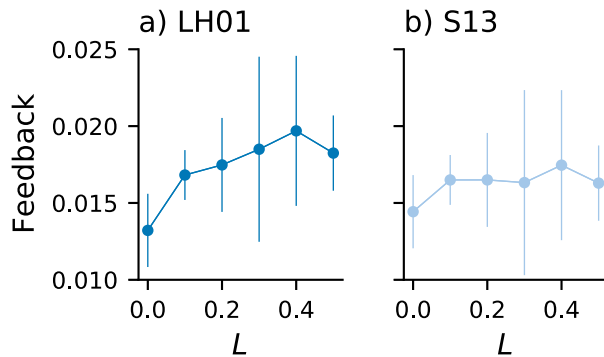


FIG. 5. (a) Strength of the positive eddy feedback γ in the dry and moist simulations, estimated using the method of Lorenz and Hartmann (2001). The markers show the average values of the γ estimates for lags of 30–60 model days and error bars show 5%–95% confidence intervals, calculated using the standard deviation of the estimates. (b) As in (a), but using the Simpson et al. (2013) method for estimating γ .

$$\frac{\partial b}{\partial t} = F(v'\theta') + F(\text{MMC}_B) - \frac{b}{\tau_d} - F(LP), \quad (12)$$

where $b = -\int(\partial/\partial y)[\theta] \cdot \mathbf{v}_\theta dy$ is the PC of the leading baroclinicity mode, $F(v'\theta') = \int(\partial^2/\partial y^2)[v'\theta'] \cdot \mathbf{v}_\theta dy$ is the forcing by the eddy heat flux divergence, $F(\text{MMC}_B) = \int -(\partial/\partial y)[\partial v_1/\partial y + \partial v_2/\partial y][\theta] \cdot \mathbf{v}_\theta dy$ is the forcing by the MMC, b/τ_d is the diabatic damping, and $F(LP) = L \int(\partial/\partial y)[P] \cdot \mathbf{v}_\theta dy$. The vector \mathbf{v}_θ is the leading EOF of the baroclinicity.

We examine the life cycles of shear and baroclinicity anomalies by regressing the terms in Eqs. (11) and (12) onto the leading shear and baroclinicity modes (s and b , respectively). Because we are interested in the low-frequency variability, we filter the data with a fourth-order low-pass Butterworth filter, using a cutoff frequency of 100 model days before performing the regressions. Blanco-Fuentes and Zurita-Gotor (2011) showed that in observations the high- and low-frequency regimes can be separated at about 10 Earth days (≈ 50 model days), but we choose a lower-frequency cutoff here because of the longer decorrelation time scales of the zonal index in the two-layer model.

We begin with the shear anomaly life cycles and the role of EMFs in Fig. 7 (for ease of presentation we only show the $L = 0, 0.2$, and 0.5 cases). In the dry case (Fig. 7a), anomalous EMFs occur about 25 days before shear maxima (Fig. 7a, dashed blue line). The anomalously strong EMFs induce an MMC that damps the shear (Fig. 7a, solid blue line) and peaks about 10 days prior to the shear maximum. This results in maximum shear at zero lag, while friction is in phase with the shear anomaly and maintains the shear past its maximum (Fig. 7a, dotted blue line). These features are consistent with the Robinson (2000) mechanism, and the dry simulations in Zurita-Gotor et al. (2014). When moisture is added the lead-lag relationships of the forcing terms are generally maintained (Figs. 7b,c), but the magnitudes of the EMF forcings weaken, such that the net forcing of shear anomalies for $L = 0.5$ reduces to about a third of the dry case.

The baroclinicity life cycles are shown in Fig. 8. In the dry case, baroclinicity anomalies are forced by the MMC, in order

to maintain thermal wind balance (Fig. 8a), and are primarily damped by diffusive EHF and, to a lesser extent, by the model's thermal relaxation (i.e., “radiation”). Hence, the EHF always acts to reduce the baroclinicity, but has a lagged response of about 20 days after the maximum baroclinicity anomaly (dashed blue line in Fig. 8a; Robinson 2000).

As already seen in the shear anomaly life cycles, the MMC weakens in the presence of moisture (Fig. 8b), leading to weaker forcing of baroclinicity anomalies, and weaker damping by the EHF and by radiation. Precipitation has a relatively small effect on the baroclinicity for small L , damping the baroclinicity at all lags, with maximum damping 25 days prior to the baroclinicity peak, roughly when the forcing by the MMC is largest. Hence precipitation responds quickly to baroclinicity perturbations induced by the MMC. The damping by precipitation is similar in all of the moist simulations and so, because the EHF weakens as L is increased, precipitation plays a leading role in damping baroclinicity anomalies for $L = 0.5$.

Lead-lag regressions of the zonal-mean precipitation onto the baroclinicity b show that the precipitation is enhanced on the poleward flank of the jet when b is anomalously strong (Fig. 9). This enhanced precipitation adds heat to the lower layer, reduces the meridional temperature gradient (see also Xia and Chang 2014), and in turn reduces the baroclinicity.

Combining the shear and baroclinicity anomaly life cycle analyses shows that the presence of moisture weakens eddy activity at all frequencies. Weaker eddies lead to weaker EMF anomalies, followed by a weaker MMC, weaker baroclinicity anomalies, and weaker zonal index z_1 anomalies, as seen in the PDFs of low-pass filtered z_1 (Fig. 6c). But despite the weaker Robinson-like dynamics, the timings of the life cycles are maintained, such that changes in γ are small.

5. Comparison with weaker mean flows

Adding moisture to the QG model damps the mean flow (Fig. 1a), which raises the question of whether it is the mean flow changes which drive the persistence changes. To isolate the effects of mean flow changes, new dry ($L = 0$) experiments were conducted in which the equilibrium jet profile in Eq. (2) was reduced by 10 and 20% (i.e., $A = 0.9$ and $A = 0.8$; see Table 1). These simulations produced comparable maximum jet speeds to the $L = 0.1$ and $L = 0.2$ simulations, respectively (see Fig. 10a), though we will focus on comparing the $L = 0.2$ and $A = 0.8$ cases. Similar results are seen when comparing the $L = 0.1$ and $A = 0.9$ cases, but the differences are smaller (not shown).

Weakening the equilibrium jet enhances the persistence of the zonal index at all lags compared to the original $A = 1$ case, but the increases are not as large as in the corresponding moist cases (Fig. 10c, Table 1). More specifically, the decay rate $d\log(C_{z_1 z_1}/d\tau)$ shows that long-lag persistence is similar, but that the short-term persistence of zonal anomalies is greater in the moist simulations (Fig. 10d).

In section 4a the enhanced short-lag persistence in the moist simulations was attributed to weaker eddy activity, which is less effective at disrupting annular mode variability. However,

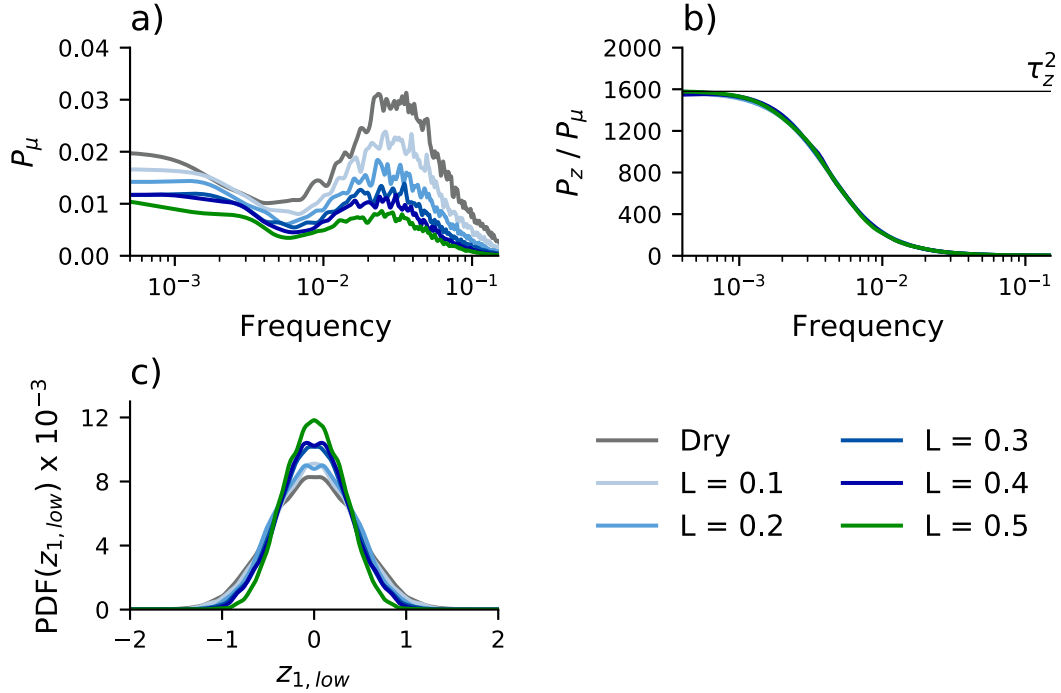


FIG. 6. (a) Power spectra of the eddy momentum forcing, μ in the experiments with $L = 0$ to 0.5. Spectra were calculated using the multitaper method, with eight spectral windows and then smoothed with a Gaussian filter. (b) Ratios of the power spectrum of the zonal index to the power spectrum of the eddy momentum forcing in the same simulations. Note that the curves nearly plot on top of each other, and are difficult to distinguish. The thin black line shows $\tau_z^2 = (2.7\tau_f)^2$. (c) Probability density functions of the low-pass filtered zonal index in the same simulations as in (a). z_1 is filtered using a third-order Butterworth filter with a cutoff frequency of 100 (model day) $^{-1}$.

Fig. 10b shows that the EKE is similar in the moist case and the corresponding dry case with a weaker mean flow—the EKE is actually slightly higher in the moist case. To investigate this further, we show PDFs of the high-pass filtered eddy momentum forcing (μ) in the $A = 0.8$ and $L = 0.2$ cases in Fig. 11a [the data are filtered to only retain power at frequencies higher than 100 (model day) $^{-1}$]. The moist PDF is slightly broader than the dry PDF, further suggesting stronger transient fluctuations and greater disruption of annular mode anomalies. Finally, lag regressions of high-pass filtered precipitation onto the zonal index indicate that latent heating damps annular mode anomalies on short time scales (not shown), consistent with the low-frequency regressions in Fig. 9. So precipitation is not the cause of the enhanced persistence in the moist simulation either.

Instead, the enhanced short-lag persistence in the moist simulations comes about because moisture is particularly effective at damping high-frequency eddies. First, comparing the power spectra of μ in the $A = 0.8$ and $L = 0.2$ cases shows that there is relatively more power at low frequencies in the $L = 0.2$ case than in the $A = 0.8$ case (Fig. 11b). Second, examining the high-frequency part of the spectra more closely shows that the moist simulation has more power at frequencies lower than 0.2 (model day) $^{-1}$, and less power at higher frequencies, compared to the dry simulation (Fig. 11c). Thus moisture damps high-frequency eddies more efficiently compared to simply weakening the mean flow, and is particularly

effective at damping very high-frequency eddies. To illustrate how this leads to enhanced annular mode persistence, we have run “offline” simulation using Eq. (8), but forced by the high-pass filtered [$>100 \text{ day}^{-1}$] eddy momentum forcing in the $A = 0.8$ and $L = 0.2$ cases. That is, we solve

$$\frac{\partial z_{1,\text{high}}}{\partial t} = \mu_{\text{high}} - \frac{z_{1,\text{high}}}{\tau_z},$$

with μ_{high} taken from the two simulations. As the thin lines in Fig. 10c show, the high-frequency forcing from the moist simulation produces a more persistence zonal index than the forcing from the dry simulation, even though the range of μ_{high} fluctuations is larger in the moist simulation (Fig. 11a).

In summary, the enhanced persistence at short lags in the moist simulations is partly due to weaker eddy activity, which is also seen in dry simulations with weaker mean flows. But the addition of moisture also damps high-frequency eddy activity more efficiently than the mean flow, particularly very high-frequency eddies (time scales < 10 days), further enhancing the persistence compared to analogous dry simulations with weaker mean flows.

6. Transition to propagating mode variability

Several studies have noted that propagating variability and associated cross-EOF feedbacks reduce annular mode

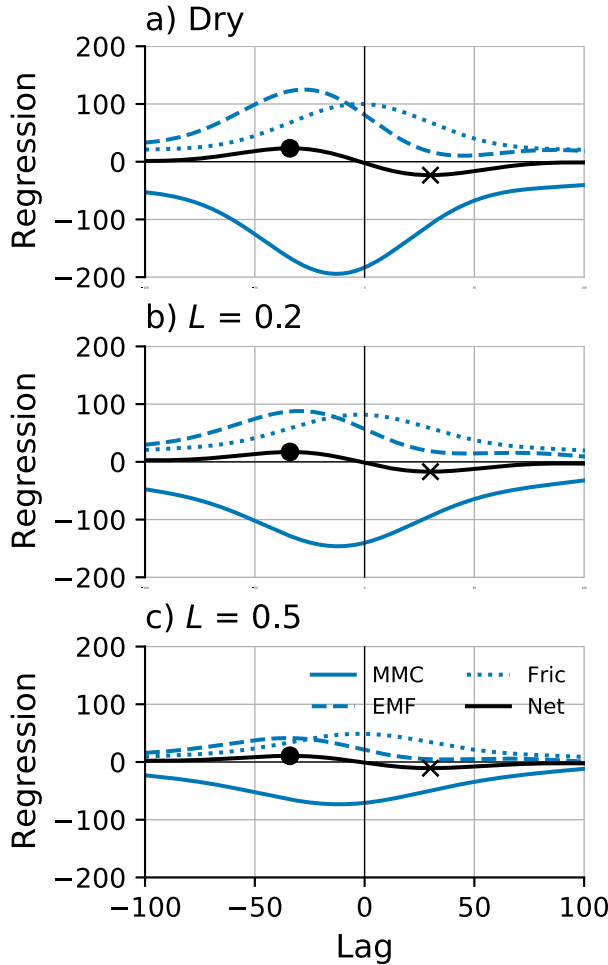


FIG. 7. (a) Regression of the terms on the right-hand side of Eq. (11) onto the anomalous shear s in the dry simulation. All data are low-pass filtered with a fourth-order Butterworth filter, using a cutoff frequency of 100 (day)^{-1} , before the regressions are performed. The solid curve shows the forcing by the MMC, the dashed curve shows the eddy momentum flux forcing, the dotted curve shows the frictional forcing, and the black curve shows the net forcing. The black circle marks the maximum net forcing and the black cross marks the minimum net forcing (the maximum net damping). The maximum shear s occurs at lag 0, and negative lags indicate that the forcing term leads the shear anomaly. (b) As in (a), but for the simulation with $L = 0.2$. (c) As in (a), but for the simulation with $L = 0.5$.

persistence (Son et al. 2008; Sheshadri and Plumb 2017; Lubis and Hassanzadeh 2021). Here, however, we find that the long-lag persistence is unchanged as the model transitions to propagating variability for large L . To understand this behavior, we follow Lubis and Hassanzadeh (2021), who extended the Lorenz and Hartmann model [Eq. (8)] to include cross-EOF feedbacks:

$$\frac{\partial z_1}{\partial t} \approx \mu_1 - \frac{z_1}{\tau_{z,1}}, \quad (13a)$$

$$\frac{\partial z_2}{\partial t} \approx \mu_2 - \frac{z_2}{\tau_{z,2}}, \quad (13b)$$

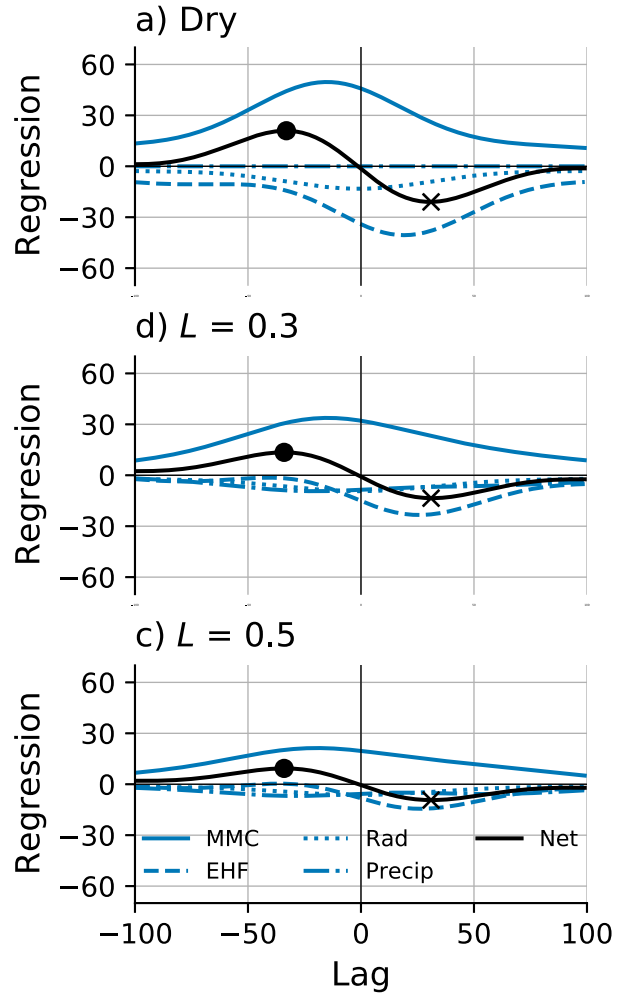


FIG. 8. (a) Regression of the terms on the right-hand side of Eq. (12) onto the anomalous baroclinicity b in the dry simulation. All data are low-pass filtered with a fourth-order Butterworth filter, using a cutoff frequency of 100 (day)^{-1} , before the regressions are performed. The solid curve shows the forcing by the MMC, the dashed curve shows the eddy heat flux forcing, the dotted curve shows the diabatic forcing, the dash-dotted curve is the forcing by precipitation, and the black curve shows the net forcing. The black circle marks the maximum net forcing and the black cross marks the minimum net forcing (the maximum net damping). The maximum baroclinicity b occurs at lag 0, and negative lags indicate that the forcing term leads the baroclinicity. (b) As in (a), but for the simulation with $L = 0.2$. (c) As in (a), but for the simulation with $L = 0.5$.

where z_2 is the principal component associated with the second EOF of the zonal-mean wind, and the momentum forcings are modeled as

$$\mu_1 = \hat{\mu}_1 + \gamma_{11}z_1 + \gamma_{12}z_2, \quad (14a)$$

$$\mu_2 = \hat{\mu}_2 + \gamma_{21}z_1 + \gamma_{22}z_2, \quad (14b)$$

with $\hat{\mu}_1$ and $\hat{\mu}_2$ denoting random eddy forcings, and γ_{12} and γ_{21} the cross-EOF feedbacks. Note that the Lorenz and Hartmann

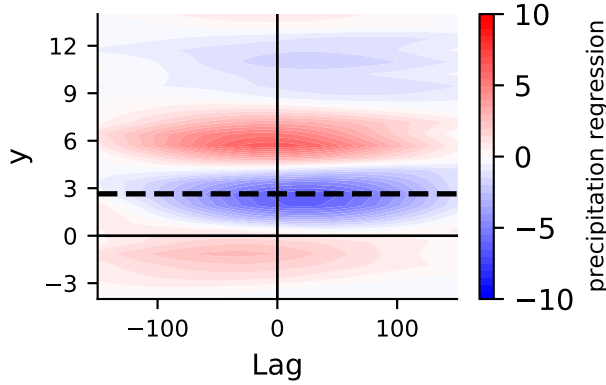


FIG. 9. Regression of low-pass filtered zonal-mean precipitation onto the low-pass filtered baroclinicity index b in the simulation with $L = 0.5$. The thick dashed black line shows the latitude of the maximum climatological zonal wind speed.

(2001) model subsumes the cross-EOF feedback γ_{12} into the γ of Eq. (8) such that the zonal index's feedback coefficient is $\gamma = \gamma_{11}z_1 + \gamma_{12}z_2/z_1$.

Building on Simpson et al. (2013), Lubis and Hassanzadeh (2021) proposed a method for estimating the feedback coefficients γ_{11} , γ_{12} , γ_{21} , and γ_{22} by lag regressing each term in Eqs. (14a) and (14b) onto z_1 and z_2 . This gives two sets of simultaneous equations, which can be solved to find the feedback coefficients:

$$\begin{bmatrix} \text{regr}(z_1, z_1) & \text{regr}(z_2, z_1) \\ \text{regr}(z_1, z_2) & \text{regr}(z_2, z_2) \end{bmatrix} \begin{bmatrix} \gamma_{11} \\ \gamma_{12} \end{bmatrix} = \begin{bmatrix} \text{regr}(\mu_1, z_1) \\ \text{regr}(\mu_1, z_2) \end{bmatrix} \quad (15)$$

and

$$\begin{bmatrix} \text{regr}(z_2, z_1) & \text{regr}(z_1, z_1) \\ \text{regr}(z_2, z_2) & \text{regr}(z_1, z_2) \end{bmatrix} \begin{bmatrix} \gamma_{21} \\ \gamma_{22} \end{bmatrix} = \begin{bmatrix} \text{regr}(\mu_2, z_1) \\ \text{regr}(\mu_2, z_2) \end{bmatrix}. \quad (16)$$

We have used this approach to estimate the eddy feedbacks and cross-EOF feedbacks in the dry and moist simulations, again calculating the regressions at lags of 30–60 model days. Even at these lags the cross-EOFs feedbacks γ_{12} and γ_{21} are noisy for small L (Fig. 12), though since these simulations are not in the propagating variability regime, γ_{12} and γ_{21} should be small.

The eddy feedback onto z_1 , γ_{11} , is roughly constant as L is varied (green circular markers in Fig. 12a), though it does appear to increase slightly, as also seen in Fig. 5. The cross-EOF feedback parameter γ_{12} is noisy for the $L < 0.4$, and then stabilizes at small positive values for $L = 0.4$ and 0.5 (light green diamonds in Fig. 12a). The second feedback parameter γ_{22} is negligible for small L , but then increases for larger L , reaching a value of roughly 0.01 for $L = 0.5$ (orange circular markers in Fig. 12b). This is consistent with the enhanced persistence of z_2 at long lags (Fig. 3f). Finally, the second cross-EOF feedback parameter γ_{21} is also noisy for the control and

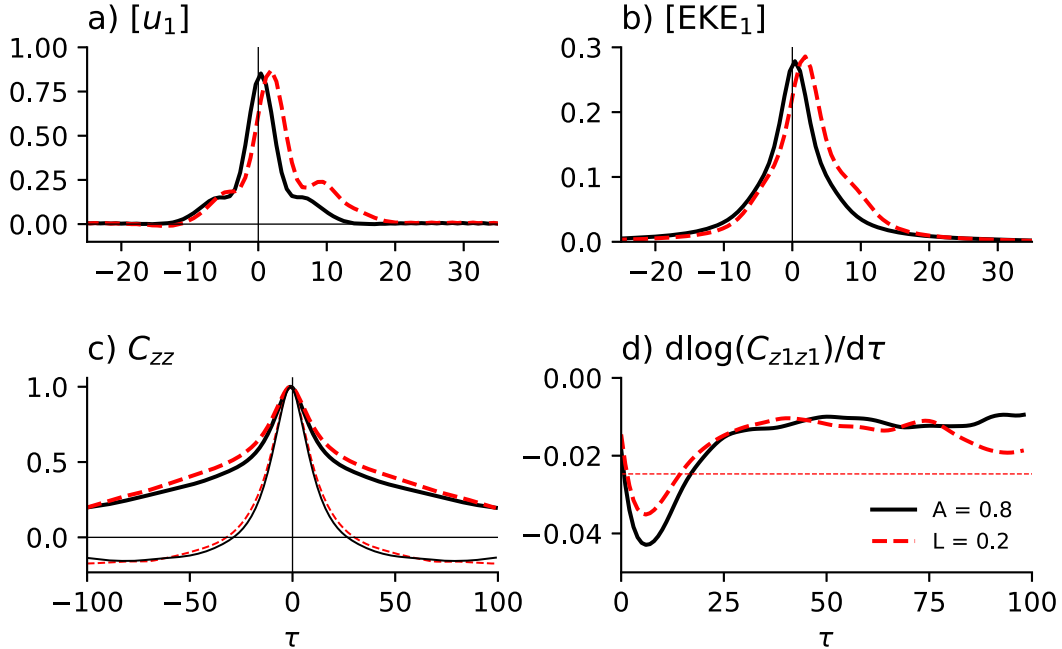


FIG. 10. (a) Climatological upper-layer zonal-mean zonal winds in the dry simulation with $A = 0.8$ (black) and the moist simulation with $L = 0.2$ (dashed red). (b) Climatological upper-layer zonal-mean eddy kinetic energy in the same simulations. (c) The autocorrelations of the principal components associated with the leading EOF in each simulation (thick lines). The thin lines show the autocorrelation of the zonal index in “offline” simulations forced by the high-pass filtered eddy momentum forcing in the $A = 0.8$ and $L = 0.2$ simulations (black and dashed red curves, respectively). See main text for more details. (d) $d \log(C_{z1z1})/d\tau$ in the same simulations. The dashed red line shows the decay rate implied by the frictional time scale τ_z .

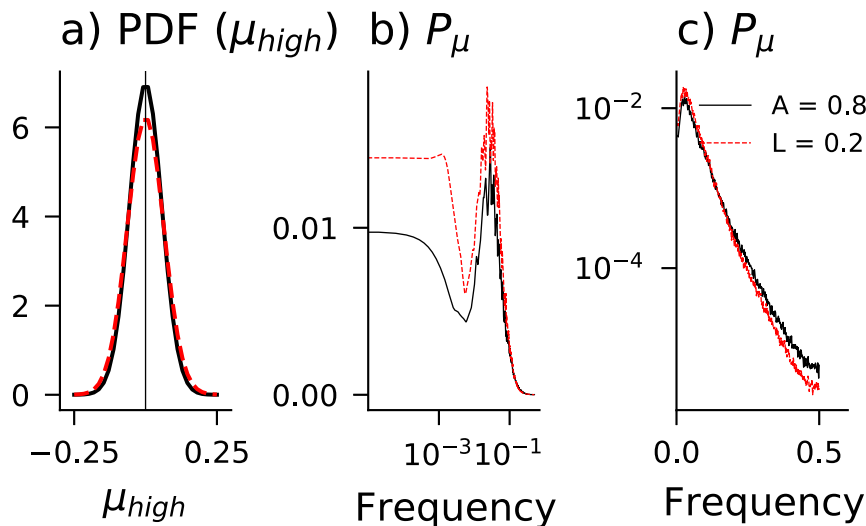


FIG. 11. (a) Probability density functions of the high-pass filtered eddy momentum forcing μ in the dry simulation with $A = 0.8$ (black) and the moist simulation with $L = 0.2$ (dashed red). μ is filtered using a third-order Butterworth filter with a cutoff frequency of 100 (model day) $^{-1}$. (b) Power spectra of the eddy momentum forcing, μ in same experiments. Spectra were calculated using the multitaper method, with eight spectral windows and then smoothed with a Gaussian filter. (c) As in (b), but using a linear scale for the x axis and a logarithmic scale for the y axis.

$L < 0.3$ simulations, but is increasingly positive for larger L (light orange diamonds in Fig. 12a).

These results are difficult to reconcile with previous work on propagating variability, which has suggested that cross-EOF feedbacks should lead to reduced long-lag persistence. Here, the changes in persistence are small as the model transitions to a propagating variability regime, and cross-EOF feedbacks do not appear to substantially alter annular mode persistence. More work is needed to understand the dynamics of cross-EOF feedbacks and to reconcile previous work in dry contexts with our moist simulations.

7. Conclusions

This study has investigated moisture's impacts on annular mode persistence. By using a two-layer QG channel model, moisture's direct effects on annular modes have been isolated, rather than the geometric effects associated with moisture-induced changes in jet latitude on the sphere. At short lags (< 20 model days, ≈ 4 Earth days), moisture enhances annular mode persistence, as weaker eddy forcing is less effective at disrupting annular mode anomalies. The weaker forcing is a consequence of the weakening of eddy activity in the presence of moisture, as discussed by Bembenek et al. (2020), though comparisons to simulations with weaker mean flows show that moisture is particularly effective at damping high-frequency eddy activity (especially very high-frequency eddies with time scales of less than ~ 10 model days), further enhancing short-lag persistence.

At longer lags, the persistence is essentially unchanged as L is varied, as the positive eddy feedback (γ) adjusts to compensate for small increases in the effective barotropic

friction at large L . The small changes in γ suggest that the large changes in baroclinicity associated with the presence of moisture have little impact on annular mode persistence.

In addition to quantifying γ , we have examined the life cycles of low-frequency baroclinic and vertical wind shear anomalies to shed light on how the dynamics underlying the positive eddy feedback respond to changes in L . We find that increasing L leads to weaker initial EMF anomalies, which induce weaker mean-flow and EHF anomalies. For larger L , precipitation becomes a leading damper of baroclinicity

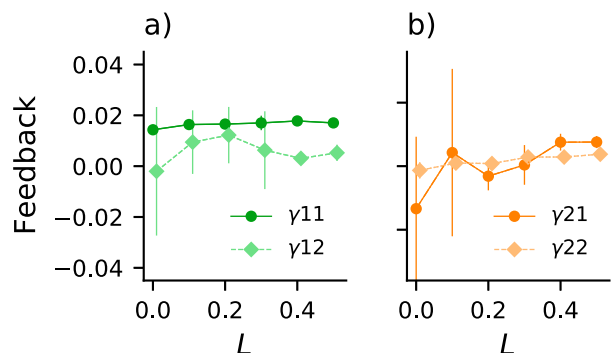


FIG. 12. (a) Eddy feedback (orange circles) and cross-EOF feedback (light orange diamonds) onto z_1 as a function of L . The feedbacks are diagnosed using Eqs. (16) and (A1) of the main text and averaged over lags of 30–60. Vertical lines show 2 times the standard deviations of the feedbacks, calculated by diagnosing the feedback at each lag from 30 to 60 days. (b) As in (a), but showing the feedbacks onto the second mode z_2 .

anomalies, and responds quickly to temperature perturbations, in contrast to the diffusive EHF which responds more slowly. But despite the weaker eddy anomalies, in all of our simulations the relative timing of the life cycles is roughly unchanged, consistent with the near-constant estimates of γ . This suggests that baroclinic dynamics do not drive annular mode persistence, and hints at a more important role for barotropic mechanisms (Jin et al. 2006b,a; Barnes and Hartmann 2011; Lorenz 2014).

The presence of moisture also promotes propagating annular mode variability, which has previously been suggested to reduce annular mode persistence, in contrast to what is seen here. More work is needed to reconcile our results with work on propagating variability in dry GCMs, to clarify the dynamics of cross-EOF feedbacks, and to relate these dynamics to the more traditional picture of the positive eddy feedback onto the leading EOF. We note that one benefit of the moist QG model for investigating these issues is that it smoothly transitions into a propagating regime as L is increased.

Given the idealized nature of our model setup, it is difficult to say which of our cases is the most realistic, though based on the scaling arguments of Lapeyre and Held (2004), we hypothesize that $L = 0.2$ is the closest. In this case the enhanced persistence at short lags results in an e -folding time scale that is roughly 21 model days (≈ 4 Earth days; Table 1) longer than in the control dry simulation. Interestingly, this suggests the absence of moisture is not the primary cause of the stronger annular mode persistence in idealized dry atmospheric models relative to observations (Gerber et al. 2008). The “shoulder” in the autocorrelation (Fig. 4a), which separates the noisy eddy forcing regime from the low-frequency eddy feedback, is also not as sharp in the presence of moisture. Many more steps are required to connect dry, idealized simulations to observed annular mode behavior, but the results presented here give a first sense for the role moisture plays in annular mode persistence.

Acknowledgments. We thank three reviewers for close readings and insightful comments that greatly improved the study. We also thank Pedram Hassanzadeh, Pablo Zurita-Gotor, and Isaac Held for helpful conversations and feedback on earlier versions of this manuscript.

APPENDIX

The Modified Time-Stepping Scheme

Adding moisture requires modifying the time-stepping scheme in the original dry model. Various new strategies were tested, but the most stable setup closely follows the approach described in the appendix of Lapeyre and Held (2004). Specifically, the time stepping proceeds in three steps: 1) The model computes the tendency terms due to dynamics and advances the PV and moisture fields. 2) The model computes P and E and adjusts moisture and PV accordingly. A modified exponential cutoff is applied to the spectral P and E fields in order to smooth the Heaviside function introduced by Eqs. (5) and (6) (see Lapeyre and Held 2004). 3) The divergence is calculated using the QG- ω equation as

$$(-\nabla^2 + 2)\nabla \cdot \mathbf{u}_2 = J(\psi_1, \zeta_1) - J(\psi_2, \zeta_2) - \nabla^2 J(\psi_2, \psi_1 - \psi_2) + \beta(v_1 - v_2) + L\nabla^2 P - \nabla^2(\psi_1 - \psi_2 - \psi_R)/\tau_d; \quad (\text{A1})$$

$\nabla \cdot \mathbf{u}_2$ is then subtracted from the moisture tendency. A sponge is also applied to m at the meridional boundaries to maintain consistency with the PV fields.

REFERENCES

- Barnes, E. A., and D. L. Hartmann, 2010: Testing a theory for the effect of latitude on the persistence of eddy-driven jets using CMIP3 simulations. *Geophys. Res. Lett.*, **37**, L15801, <https://doi.org/10.1029/2010GL044144>.
- , and —, 2011: Rossby wave scales, propagation, and the variability of eddy-driven jets. *J. Atmos. Sci.*, **68**, 2893–2908, <https://doi.org/10.1175/JAS-D-11-039.1>.
- Bembenek, E., D. N. Straub, and T. M. Merlis, 2020: Effects of moisture in a two-layer model of the midlatitude jet stream. *J. Atmos. Sci.*, **77**, 131–147, <https://doi.org/10.1175/JAS-D-19-0021.1>.
- Blanco-Fuentes, J., and P. Zurita-Gotor, 2011: The driving of baroclinic anomalies at different timescales. *Geophys. Res. Lett.*, **38**, L23805, <https://doi.org/10.1029/2011GL049785>.
- Bouchut, F., J. Lambaerts, G. Lapeyre, and V. Zeitlin, 2009: Fronts and nonlinear waves in a simplified shallow-water model of the atmosphere with moisture and convection. *Phys. Fluids*, **21**, 116604, <https://doi.org/10.1063/1.3265970>.
- Byrne, N. J., T. G. Shepherd, T. Woollings, and R. A. Plumb, 2016: Annular modes and apparent eddy feedbacks in the Southern Hemisphere. *Geophys. Res. Lett.*, **43**, 3897–3902, <https://doi.org/10.1002/2016GL068851>.
- Chang, E. K. M., and S. Song, 2006: The seasonal cycles in the distribution of precipitation around cyclones in the western North Pacific and Atlantic. *J. Atmos. Sci.*, **63**, 815–839, <https://doi.org/10.1175/JAS3661.1>.
- Feldstein, S., and S. Lee, 1998: Is the atmospheric zonal index driven by an eddy feedback? *J. Atmos. Sci.*, **55**, 3077–3086, [https://doi.org/10.1175/1520-0469\(1998\)055<3077:ITAZID>2.0.CO;2](https://doi.org/10.1175/1520-0469(1998)055<3077:ITAZID>2.0.CO;2).
- Frierson, D. M. W., I. M. Held, and P. Zurita-Gotor, 2006: A gray-radiation aquaplanet moist GCM. Part I: Static stability and eddy scale. *J. Atmos. Sci.*, **63**, 2548–2566, <https://doi.org/10.1175/JAS3753.1>.
- Gerber, E. P., and G. K. Vallis, 2007: Eddy–zonal flow interactions and the persistence of the zonal index. *J. Atmos. Sci.*, **64**, 3296–3311, <https://doi.org/10.1175/JAS4006.1>.
- , S. Voronin, and L. M. Polvani, 2008: Testing the annular mode autocorrelation time scale in simple atmospheric general circulation models. *Mon. Wea. Rev.*, **136**, 1523–1536, <https://doi.org/10.1175/2007MWR2211.1>.
- Hartmann, D. L., and F. Lo, 1998: Wave-driven zonal flow vacillation in the Southern Hemisphere. *J. Atmos. Sci.*, **55**, 1303–1315, [https://doi.org/10.1175/1520-0469\(1998\)055<1303:WDZFVI>2.0.CO;2](https://doi.org/10.1175/1520-0469(1998)055<1303:WDZFVI>2.0.CO;2).
- Hassanzadeh, P., and Z. Kuang, 2016: The linear response function of an idealized atmosphere. Part II: Implications for the practical use of the fluctuation–dissipation theorem and the role of operator’s nonnormality. *J. Atmos. Sci.*, **73**, 3441–3452, <https://doi.org/10.1175/JAS-D-16-0099.1>.
- , and —, 2019: Quantifying the annular mode dynamics in an idealized atmosphere. *J. Atmos. Sci.*, **76**, 1107–1124, <https://doi.org/10.1175/JAS-D-18-0268.1>.

- Held, I. M., and M. Zhao, 2008: Horizontally homogeneous rotating radiative–convective equilibria at GCM resolution. *J. Atmos. Sci.*, **65**, 2003–2013, <https://doi.org/10.1175/2007JAS2604.1>.
- Jin, F.-F., L.-L. Pan, and M. Watanabe, 2006a: Dynamics of synoptic eddy and low-frequency flow interaction. Part I: A linear closure. *J. Atmos. Sci.*, **63**, 1677–1694, <https://doi.org/10.1175/JAS3715.1>.
- , —, and —, 2006b: Dynamics of synoptic eddy and low-frequency flow interaction. Part II: A theory for low-frequency modes. *J. Atmos. Sci.*, **63**, 1695–1708, <https://doi.org/10.1175/JAS3716.1>.
- Lainé, A., G. Lapeyre, and G. Rivière, 2011: A quasigeostrophic model for moist storm tracks. *J. Atmos. Sci.*, **68**, 1306–1322, <https://doi.org/10.1175/2011JAS3618.1>.
- Lambaerts, J., G. Lapeyre, and V. Zeitlin, 2011a: Moist versus dry barotropic instability in a shallow-water model of the atmosphere with moist convection. *J. Atmos. Sci.*, **68**, 1234–1252, <https://doi.org/10.1175/2011JAS3540.1>.
- , —, —, and F. Bouchut, 2011b: Simplified two-layer models of precipitating atmosphere and their properties. *Phys. Fluids*, **23**, 046603, <https://doi.org/10.1063/1.3582356>.
- , —, and —, 2012: Moist versus dry baroclinic instability in a simplified two-layer atmospheric model with condensation and latent heat release. *J. Atmos. Sci.*, **69**, 1405–1426, <https://doi.org/10.1175/JAS-D-11-0205.1>.
- Lapeyre, G., and I. M. Held, 2004: The role of moisture in the dynamics and energetics of turbulent baroclinic eddies. *J. Atmos. Sci.*, **61**, 1693–1710, [https://doi.org/10.1175/1520-0469\(2004\)061<1693:TROMIT>2.0.CO;2](https://doi.org/10.1175/1520-0469(2004)061<1693:TROMIT>2.0.CO;2).
- Lorenz, D. J., 2014: Understanding midlatitude jet variability and change using Rossby wave chromatography: Wave–mean flow interaction. *J. Atmos. Sci.*, **71**, 3684–3705, <https://doi.org/10.1175/JAS-D-13-0201.1>.
- , and D. L. Hartmann, 2001: Eddy–zonal flow feedback in the Southern Hemisphere. *J. Atmos. Sci.*, **58**, 3312–3327, [https://doi.org/10.1175/1520-0469\(2001\)058<3312:EZFFIT>2.0.CO;2](https://doi.org/10.1175/1520-0469(2001)058<3312:EZFFIT>2.0.CO;2).
- Lubis, S., and P. Hassanzadeh, 2021: An eddy–zonal flow feedback model for propagating annular modes. *J. Atmos. Sci.*, **78**, 249–267, <https://doi.org/10.1175/JAS-D-20-0214.1>.
- Lutsko, N. J., I. M. Held, and P. Zurita-Gotor, 2015: Applying the fluctuation–dissipation theorem to a two-layer model of quasigeostrophic turbulence. *J. Atmos. Sci.*, **72**, 3161–3177, <https://doi.org/10.1175/JAS-D-14-0356.1>.
- , —, —, and A. K. O'Rourke, 2017: Lower-tropospheric eddy momentum fluxes in idealized models and reanalysis data. *J. Atmos. Sci.*, **74**, 3787–3797, <https://doi.org/10.1175/JAS-D-17-0099.1>.
- Ma, D., P. Hassanzadeh, and Z. Kuang, 2017: Quantifying the eddy–jet feedback strength of the annular mode in an idealized GCM and reanalysis data. *J. Atmos. Sci.*, **74**, 393–407, <https://doi.org/10.1175/JAS-D-16-0157.1>.
- Monahan, A. H., and J. C. Fyfe, 2006: On the nature of zonal jet EOFs. *J. Climate*, **19**, 6409–6424, <https://doi.org/10.1175/JCLI3960.1>.
- , and —, 2009: How generic are dipolar jet EOFs? *J. Atmos. Sci.*, **66**, 541–551, <https://doi.org/10.1175/2008JAS2814.1>.
- North, G. R., T. L. Bell, R. F. Calahan, and F. J. Moeng, 1982: Sampling errors in the estimation of empirical orthogonal functions. *Mon. Wea. Rev.*, **110**, 699–706, [https://doi.org/10.1175/1520-0493\(1982\)110<0699:SEITEO>2.0.CO;2](https://doi.org/10.1175/1520-0493(1982)110<0699:SEITEO>2.0.CO;2).
- Ring, M. J., and R. A. Plumb, 2008: The response of a simplified GCM to axisymmetric forcings: Applicability of the fluctuation–dissipation theorem. *J. Atmos. Sci.*, **65**, 3880–3898, <https://doi.org/10.1175/2008JAS2773.1>.
- Robinson, W. A., 2000: A baroclinic mechanism for the eddy feedback on the zonal index. *J. Atmos. Sci.*, **57**, 415–422, [https://doi.org/10.1175/1520-0469\(2000\)057<0415:ABMFTE>2.0.CO;2](https://doi.org/10.1175/1520-0469(2000)057<0415:ABMFTE>2.0.CO;2).
- Sheshadri, A., and R. A. Plumb, 2017: Propagating annular modes: Empirical orthogonal functions, principal oscillation patterns, and time scales. *J. Atmos. Sci.*, **74**, 1345–1361, <https://doi.org/10.1175/JAS-D-16-0291.1>.
- Simpson, I. R., T. G. Shepherd, P. Hitchcock, and J. F. Scinocca, 2013: Southern annular mode dynamics in observations and models. Part II: Eddy feedbacks. *J. Climate*, **26**, 5220–5241, <https://doi.org/10.1175/JCLI-D-12-00495.1>.
- Son, S.-W., and S. Lee, 2006: Preferred modes of variability and their relationship with climate change. *J. Climate*, **19**, 2063–2075, <https://doi.org/10.1175/JCLI3705.1>.
- , —, S. B. Feldstein, and J. E. T. Hovee, 2008: Time scale and feedback of zonal–mean–flow variability. *J. Atmos. Sci.*, **65**, 935–952, <https://doi.org/10.1175/2007JAS2380.1>.
- Thompson, D. W. J., and J. M. Wallace, 2000: Annular modes in the extratropical circulation. Part I: Month-to-month variability. *J. Climate*, **13**, 1000–1016, [https://doi.org/10.1175/1520-0442\(2000\)013<1000:AMITEC>2.0.CO;2](https://doi.org/10.1175/1520-0442(2000)013<1000:AMITEC>2.0.CO;2).
- , and E. A. Barnes, 2014: Periodic variability in the large-scale Southern Hemisphere atmospheric circulation. *Science*, **343**, 641–645, <https://doi.org/10.1126/science.1247660>.
- Wernli, H., and H. C. Davies, 1997: A Lagrangian-based analysis of extratropical cyclones. I: The method and some applications. *Quart. J. Roy. Meteor. Soc.*, **123**, 467–489, <https://doi.org/10.1002/qj.49712353811>.
- Xia, X., and E. K. M. Chang, 2014: Diabatic damping of zonal index variations. *J. Atmos. Sci.*, **71**, 3090–3105, <https://doi.org/10.1175/JAS-D-13-0292.1>.
- Zhou, W., I. M. Held, and S. T. Garner, 2017: Tropical cyclones in rotating radiative–convective equilibrium with coupled SST. *J. Atmos. Sci.*, **74**, 879–892, <https://doi.org/10.1175/JAS-D-16-0195.1>.
- Zurita-Gotor, P., 2014: On the sensitivity of zonal-index persistence to friction. *J. Atmos. Sci.*, **71**, 3788–3800, <https://doi.org/10.1175/JAS-D-14-0067.1>.
- , J. Blanco-Fuentes, and E. P. Gerber, 2014: The impact of baroclinic eddy feedback on the persistence of jet variability in the two-layer model. *J. Atmos. Sci.*, **71**, 410–429, <https://doi.org/10.1175/JAS-D-13-0102.1>.